Computational Materials Science 164 (2019) 116–126

Contents lists available at ScienceDirect

Computational Materials Science

journal homepage: www.elsevier.com/locate/commatsci

Impact of solutes on the lattice parameters and elastic stiffness coefficients of hcp Fe from first-principles calculations

Michael R. Fellinger[a,*], Louis G. Hector Jr[b], Dallas R. Trinkle[a]

[a] Department of Materials Science and Engineering, University of Illinois at Urbana-Champaign, Urbana, IL 61801, USA
[b] General Motors Global R&D Center, 30470 Harley Earl Blvd, Warren, MI 48092, USA

ARTICLE INFO

Keywords:
Lattice parameters
Elastic constants
Solutes
Iron
Steel
hcp
Martensite
Ab initio
DFT

ABSTRACT

The hexagonal close-packed (hcp) ε-martensite phase in steels nucleates from the γ-austenite parent phase and can undergo further transformation to the α'-martensite phase or exist as a metastable phase depending on temperature, mechanical loading, and alloy chemistry. The solute-dependent lattice parameters and elastic stiffness coefficients C_{ij} of hcp Fe influence the mechanical properties of steels containing the ε-martensite phase, as well as the martensitic transformations between the phases. We use density functional theory to calculate the lattice parameters and C_{ij} of single-crystal hcp Fe as functions of solute concentration in the dilute limit for the substitutional solutes Al, B, Cu, Mn, and Si, and the octahedral interstitial solutes C and N. Our computationally efficient methodology separates the solute dependence of the C_{ij} into lattice strain and chemical bonding contributions. The computed data can be used to estimate the effect of solutes on polycrystalline elastic moduli and the strain energy associated with martensitic transformations. The data can also serve as inputs to microstructure-based models of multiphase steels containing the ε-martensite phase.

1. Introduction

Steel alloys find widespread application as structural materials since they are cost-effective and their mechanical properties can be tuned through processing and alloying more easily than many other structural materials [1,2]. The most common phases found in structural steels for automotive applications include α-ferrite (body-centered cubic), γ-austenite (face-centered cubic), and α'-martensite (body-centered tetragonal). The hexagonal close-packed (hcp) phase of pure Fe (space group $P6_3/mmc$) is non-magnetic and is stable at high pressure, but can also form from the γ-austenite phase during a stress-assisted [3–8] or strain-induced [9] martensitic transformation. The transformed austenite can be stabilized by solute additions [10–12] leading to the hcp ε-martensite phase found in some steels, or it can further transform to the α'-martensite phase [4–7,13–17] depending on temperature, mechanical deformation, and alloy chemistry. The ε-martensite phase occurs at the intersection of shear bands in some transformation-induced plasticity (TRIP) steels [8,18–21], can form after plastic deformation in twinning-induced plasticity (TWIP) steels [20,22] and stainless steels [7,9,13,16,17,23–27], and is also found in FeMn-based shape memory alloys [28–38]. Experimental measurements on a variety of steels [3,13,16,23,24,39–44] show that the α'-martensite phase can nucleate at the intersection of two ε-martensite laths or inside a single ε-martensite lath during the $\gamma \rightarrow \varepsilon \rightarrow \alpha'$ martensitic transformation. Iron alloys with the ε-martensite phase typically contain Al, C, Co, Cr, Mn, Ni, and Si solutes [8,19,21,22,27,37].

In addition to governing mechanical properties of multiphase steels [45,46], the lattice parameters and elastic stiffness coefficients C_{ij} of γ-austenite, ε-martensite, and α'-martensite influence the martensitic transformations between these phases [16,17,20,47,48]. The lattice parameters and C_{ij} determine the strain energy contributions to the free energy difference between the parent and product phases [4,47,48], govern the structure and energy of the interfacial regions between phases [4,16,48], and control the separation between Shockley partial dislocations that can glide to produce the martensitic transformations [3–5,15–17,48]. The lattice parameters and C_{ij} of Fe phases depend on the concentration of solutes in the alloy [49–53], so understanding the influence of solutes on the structural and elastic properties of hcp Fe is crucial for modelling the formation, mechanical stability, and subsequent transformation of the ε-martensite phase. Solute-dependent lattice parameters and C_{ij} of hcp Fe also serve to increase the accuracy and predictive capabilities of microstructure-based simulations of the elastic [54] and plastic [46,55] response of Fe-based shape memory alloys and multiphase steels containing ε-martensite.

Most experimental and theoretical studies of solute effects on the lattice parameters and elasticity of Fe alloys have focused on either

* Corresponding author.
E-mail address: mfelling@illinois.edu (M.R. Fellinger).

https://doi.org/10.1016/j.commatsci.2019.03.056
Received 15 February 2019; Received in revised form 28 February 2019; Accepted 26 March 2019

polycrystalline steels [49], or single crystals with the body-centered cubic (ferrite) [50,52,56] or body-centered tetragonal (α'-martensite) structure [53,56–58]. While first-principles methods have been used to compute the structural and elastic properties of pure single-crystal hcp Fe [59–62] and the effect of Si and C solutes on the elasticity of hcp Fe [63–65], these previous studies largely focused on behavior at pressures relevant to the Earth's core (~ 360 GPa), rather than the low pressures that occur in most structural steel applications where the elastic stiffness is generally much lower [63]. We therefore present a detailed density functional theory (DFT) study of the effects of Al, B, C, Cu, Mn, N, and Si solutes commonly found in high-strength steels for automotive applications on the single-crystal lattice parameters and C_{ij} of hcp Fe at zero pressure. Our computationally efficient approach determines the changes in the C_{ij} due to the separate effects of solute-induced strain and changes in chemical bonding around the solutes [52,53]. We also provide estimates of the effect of these solutes on the polycrystalline elastic moduli of hcp Fe, and discuss how solutes influence the strain energy associated with the ε to α' transformation.

The rest of this paper is organized as follows. Section 2 gives the details of our DFT calculations and discusses our models for the solute dependence of the lattice parameters and C_{ij} of hcp Fe in the dilute limit. Section 3 presents our results for the variation of the lattice parameters and C_{ij} with solute concentration. Here we also compute the effect of solutes on the volumetric strain difference between the ε and α' phases in steels, and discuss the implications for the martensitic transformation between these phases. Section 4 summarizes the results and provides further discussion. The Appendix gives expressions for the elastic moduli of polycrystalline hcp Fe and their derivatives with respect to solute concentration in terms of the derivatives of the single-crystal C_{ij}.

2. Computational methods

We use DFT to compute the lattice parameters and C_{ij} of non-magnetic hcp Fe as functions of the concentration of Al, B, C, Cu, Mn, N, and Si solutes in the dilute limit. We treat Al, Cu, Mn, and Si as substitutional solutes. We compute the formation energies of B, C, and N in substitutional and six different interstitial sites, and show that B is most energetically stable as a substitutional solute whereas C and N are most energetically stable as octahedral interstitial solutes.

2.1. DFT calculation details

All of our DFT calculations are performed using the plane-wave basis code VASP [66]. We use the PBE generalized gradient approximation (GGA) functional [67] for the electron exchange-correlation energy, and projector augmented wave (PAW) potentials [68] generated by Kresse and Joubert [69] to model the nuclei and core electrons of Fe and all of the solutes. The PAW potentials for Fe, Al, B, Cu, Mn, Si, C, and N have the respective electronic configurations [Ar]$3d^7 4s^1$, [Ne]$3s^2 3p^1$, [He]$2s^2 2p^1$, [Ar]$3d^{10} 4s^1$, [Ar]$3d^6 4s^1$, [Ne]$3s^2 3p^2$, [He]$2s^2 2p^2$, and [He]$2s^2 2p^3$. The calculations require a plane-wave energy cutoff of 550 eV to converge the energies to less than 1 meV/atom. The energy tolerance for the electronic self-consistency loop is 10^{-8} eV, and we use a conjugate gradient method to relax the atoms until all of the atomic forces are less than 5 meV/Å. The k-point meshes for our $4 \times 4 \times 3$ supercell calculations are based on a $32 \times 32 \times 20$ unit cell k-point mesh. We use order-one Methfessel-Paxton smearing [70] to ensure accurate forces and stresses for relaxing supercells and calculating the C_{ij}. For our chosen k-point density, we use a smearing energy width of 0.2 eV to ensure close agreement between the smeared electronic density of states near the Fermi energy and the electronic density of states computed using the linear tetrahedron method with Blöchl corrections [71]. We use standard stress-strain calculations to compute the C_{ij} [52,53,72,73], taking care to fully relax the atomic positions after applying strain [61,74,75]. We use standard finite difference formulas to compute derivatives of the C_{ij} with respect to lattice parameters or solute concentrations [52,53,76].

We model hcp Fe as non-magnetic since we find that the ferromagnetic state and several different antiferromagnetic magnetic states relax to the non-magnetic state at zero pressure. The ground state magnetic structure of hcp Fe at zero pressure was also found to be non-magnetic in previous DFT-GGA calculations [60,61]. Experiments show that the hcp ε-martensite phase in steels is not magnetizable [2], and Mössbauer effect studies on Fe-Mn alloys [77,78] suggest that the hcp phase is paramagnetic but that the magnetic moments on the Fe atoms are all less than 0.1 μ_B [78]. Furthermore, *ab inito* simulations of hcp Fe-Mn random alloys within the disordered local moment (DLM) approximation for paramagnetism [51] show that the local Fe magnetic moments are zero at the equilibrium volume. All of the solutes in our study are also non-magnetic, with the possible exception of Mn. We performed test calculations where we initialized the Mn magnetic moment to a non-zero value, and we found that after relaxation the moment goes to approximately zero. The DLM study on hcp Fe-Mn alloys in Ref. [51] also found that the local magnetic moments on the Mn atoms are zero at the equilibrium volume. We therefore treated Mn as non-magnetic in all subsequent calculations.

2.2. Solute formation energy calculations

We perform formation energy calculations to show that C and N are most stable as octahedral interstitial solutes, whereas B is most stable as a substitutional solute. The formation energy of substitutional solutes is computed as

$$E^{\mathrm{f}}_{\mathrm{sub}} = E[(N-1)\mathrm{Fe}, s_{\mathrm{sub}}] - (N-1)E[N\mathrm{Fe}]/N - E[s], \tag{1}$$

where $E[(N-1)\mathrm{Fe}, s_{\mathrm{sub}}]$ is the total energy of a supercell containing $(N-1)$ Fe atoms and a solute s at a substitutional site, $E[N\mathrm{Fe}]$ is the total energy of a supercell containing N Fe atoms, and $E[s]$ is the energy of a single solute atom. The formation energy of interstitial solutes is computed as

$$E^{\mathrm{f}}_{\mathrm{int}} = E[N\mathrm{Fe}, s_{\mathrm{int}}] - E[N\mathrm{Fe}] - E[s], \tag{2}$$

where $E[N\mathrm{Fe}, s_{\mathrm{int}}]$ is the total energy of a supercell containing N Fe atoms and a solute s at an interstitial site. Since we are interested in the relative stability of the solutes at different sites within the crystal, we compute the interstitial formation energies $E^{\mathrm{f,rel}}_{\mathrm{int}}$ relative to the substitutional formation energy for each solute

$$E^{\mathrm{f,rel}}_{\mathrm{int}} = E^{\mathrm{f}}_{\mathrm{int}} - E^{\mathrm{f}}_{\mathrm{sub}}. \tag{3}$$

Table 1 compares $E^{\mathrm{f,rel}}_{\mathrm{int}}$ for interstitial solutes at octahedral, tetrahedral, hexahedral, face-centered, basal crowdion, and non-basal crowdion interstitial sites [79,80].

2.3. Effect of solutes on lattice parameters and elastic stiffness coefficients

We compute the solute dependence of the hcp Fe lattice parameters a_k and elastic stiffness coefficients C_{ij} in the dilute limit using a DFT-

Table 1
Formation energies for B, C, and N solutes at six different interstitial sites relative to the substitutional formation energy of each solute. We consider octahedral (oct), tetrahedral (tet), hexahedral (hex), face-centered (fc), basal crowdion (bc), and non-basal crowdion (nbc) interstitial sites in the hcp lattice. B is the most stable as a substitutional solute, whereas C and N are the most stable as interstitial octahedral solutes.

Solute	$E^{\mathrm{f,rel}}_{\mathrm{oct}}$	$E^{\mathrm{f,rel}}_{\mathrm{tet}}$	$E^{\mathrm{f,rel}}_{\mathrm{hex}}$	$E^{\mathrm{f,rel}}_{\mathrm{fc}}$	$E^{\mathrm{f,rel}}_{\mathrm{bc}}$	$E^{\mathrm{f,rel}}_{\mathrm{nbc}}$
B	+0.70 eV	+2.62	+2.52	+1.88	+1.88	+ 1.88
C	−2.07	−0.30	−0.44	−0.58	−0.44	− 0.54
N	−3.14	−2.06	−1.95	−1.71	−1.95	− 1.47

based methodology that closely follows the approach we developed for cubic [52] and tetragonal crystal structures [53]. Here we summarize the approach and refer the reader to Refs. [52,53] for more details. In this study, $a_1 = a_2$ are equal to the hcp lattice parameter conventionally denoted as a, and a_3 is equal to the hcp lattice parameter conventionally denoted as c (i.e., we are using three-index Bravais notation, rather than four-index Miller-Bravais notation). In the dilute limit the a_k and C_{ij} depend linearly on solute concentration c_s [49,52,53,81–83],

$$a_k(\{c_s\}) = a_k^0 + \sum_s \left.\frac{\partial a_k}{\partial c_s}\right|_{c_s=0} \cdot c_s + ..., \tag{4}$$

$$C_{ij}(\{c_s\}) = C_{ij}^0 + \sum_s \left(\frac{\partial C_{ij}}{\partial c_s}\right)_{\text{tot}} \cdot c_s + ..., \tag{5}$$

where a_k^0 and C_{ij}^0 are the lattice parameters and elastic stiffness coefficients of pure hcp Fe, respectively, and the sums are over solute species. The total derivative of C_{ij} in Eq. (5) is

$$\left(\frac{\partial C_{ij}}{\partial c_s}\right)_{\text{tot}} = \left(\frac{\partial C_{ij}}{\partial c_s}\right)_{\text{strain}} + \left(\frac{\partial C_{ij}}{\partial c_s}\right)_{\text{chem}}, \tag{6}$$

where the first term on the right is the solute-induced strain contribution and the second term is the contribution from changes in chemical bonding around the solute atom. In the following sections we give expressions for the derivatives in Eqs. (4) and (6), where we denote the DFT approximation of a physical quantity X as $\widetilde{X}$.

2.3.1. Derivative of a_k with respect to c_s

The solute dependence of the lattice parameter a_k arises from the stress the solutes induce in the host crystal and the strain the crystal undergoes to relieve this stress. We compute the derivative of a_k with respect to c_s in the dilute limit from the solute strain misfit tensor ε_{ij}^s, which is the derivative of solute-induced strain $e_{ij}^{c_s}$ with respect to solute concentration c_s [52,53],

$$\varepsilon_{ij}^s = \left.\frac{\partial e_{ij}^{c_s}}{\partial c_s}\right|_{c_s=0}. \tag{7}$$

The substitutional and octahedral interstitial solutes considered in this study do not induce shear strain in hcp Fe, so the off-diagonal elements of ε_{ij}^s are zero. The derivative of the lattice parameter a_i with respect to c_s is determined from

$$\varepsilon_{ij}^s = \frac{1}{a_i^0}\left.\frac{\partial a_i}{\partial c_s}\right|_{c_s=0} \delta_{ij}(\delta_{i1} + \delta_{i2} + \delta_{i3}), \tag{8}$$

where δ_{ij} is the Kronecker delta.

We compute ε_{ij}^s from the elastic compliance tensor of the host crystal S_{ijkl}^0, and the solute's elastic dipole tensor P_{kl}^s [84] which captures the stress the solute induces in the host crystal. The DFT approximation to P_{kl}^s is [53,84]

$$\widetilde{P}_{kl}^s = -N\Omega_0\sigma_{kl}^{(s,N,\Omega_0)}, \tag{9}$$

where N is the number of lattice sites in the computational supercell, Ω_0 is the volume per atom in the ideal solute-free hcp crystal, and $\sigma_{kl}^{(s,N,\Omega_0)}$ is the DFT-computed stress that a single solute induces in the supercell with fixed ideal hcp lattice vectors after relaxing the atomic positions. To ensure that only solute-induced stress is included in Eq. (9), any small residual stress computed for the solute-free supercell should be subtracted from $\sigma_{kl}^{(s,N,\Omega_0)}$ which is computed for the supercell containing a solute. The DFT approximation to ε_{ij}^s is then [52,53]

$$\widetilde{\varepsilon}_{ij}^s = -\frac{1}{\Omega_0}\sum_{k,l} S_{ijkl}^0 \widetilde{P}_{kl}^s, \tag{10}$$

or explicitly for substitutional and octahedral interstitial solutes,

$$\widetilde{\varepsilon}_{ij}^s = -\frac{1}{\Omega_0}[(S_{1111}^0 + S_{1122}^0)\widetilde{P}_{11}^s + S_{1122}^0\widetilde{P}_{33}^s]\delta_{ij}(\delta_{i1} + \delta_{i2}) - \frac{1}{\Omega_0}[2S_{1122}^0\widetilde{P}_{11}^s + S_{1111}^0\widetilde{P}_{33}^s]\delta_{ij}\delta_{i3}. \tag{11}$$

For selected solutes we verify the accuracy of Eq. (11) by fully relaxing the atomic and lattice degrees of freedom of the supercells and directly computing the diagonal components of the solute strain misfit tensors as

$$\widetilde{\varepsilon}_{kk}^s = N(a_k^s - a_k^0)/a_k^0, \tag{12}$$

where a_k^s is a fully relaxed lattice parameter of the supercell containing a solute. Computing ε_{kk}^s using Eq. (11) is more computationally efficient, however, since it requires relaxing only the atomic degree of freedom, whereas Eq. (12) requires relaxing both the atomic and lattice degrees of freedom.

2.3.2. Derivatives of the C_{ij} with respect to c_s

The solute dependence of the elastic stiffness coefficients C_{ij} arises from the solute-induced strain that changes the lattice parameters of the host crystal, and the local changes in chemical bonding around the solutes [52,53] (see Eq. (6)). For both substitutional and interstitial solutes, there are strain contributions from changes in the a_1 basal lattice parameter and from changes in the a_3 lattice parameter (i.e., along the c-axis). The strain contribution is the sum of the derivatives of the solute-free hcp Fe C_{ij}^0 with respect to the lattice parameters times the derivatives of the lattice parameters with respect to solute concentration,

$$\left(\frac{\partial C_{ij}}{\partial c_s}\right)_{\text{strain}} = \sum_{k=1}^{2}\left(\left.\frac{\partial C_{ij}^0}{\partial a_k}\right|_{a_k=a_k^0} \cdot \left.\frac{\partial a_k}{\partial c_s}\right|_{c_s=0}\right) + \left.\frac{\partial C_{ij}^0}{\partial a_3}\right|_{a_3=a_3^0} \cdot \left.\frac{\partial a_3}{\partial c_s}\right|_{c_s=0}, \tag{13}$$

$$\left(\frac{\partial \widetilde{C_{ij}}}{\partial c_s}\right)_{\text{strain}} = \sum_{k=1}^{2}\left(\left.\frac{\partial \widetilde{C_{ij}^0}}{\partial a_k}\right|_{a_k=a_k^0} \cdot a_k^0\varepsilon_{kk}^s\right) + \left.\frac{\partial \widetilde{C_{ij}^0}}{\partial a_3}\right|_{a_3=a_3^0} \cdot a_3^0\varepsilon_{33}^s, \tag{14}$$

where the DFT approximations for $\partial C_{ij}^0/\partial a_k$ and $\partial C_{ij}^0/\partial a_3$ in Eq. (14) are computed using a four-point central finite difference method (see Refs. [52,53] for details). In practice we do not compute the two separate derivatives of the C_{ij}^0 in the sum in Eq. (14) (i.e., for $k = 1$ and 2), but rather compute the C_{ij}^0 derivatives after applying uniform basal strain to the lattice. The chemical contribution in Eq. (6) is

$$\left(\frac{\partial C_{ij}}{\partial c_s}\right)_{\text{chem}} = \left.\frac{\partial C_{ij}}{\partial c_s}\right|_{\substack{\Omega=\Omega_0 \\ c_s=0}}. \tag{15}$$

We approximate this derivative using a forward finite difference,

$$\left(\frac{\partial \widetilde{C_{ij}}}{\partial c_s}\right)_{\text{chem}} = N[C_{ij}^s(\Omega_0) - C_{ij}^0], \tag{16}$$

where $C_{ij}^s(\Omega_0)$ is an elastic stiffness coefficient of an hcp Fe crystal that contains solute s but has the lattice parameters of ideal solute-free hcp Fe. We compute $C_{ij}^s(\Omega_0)$ by applying strain to supercells that contain a single solute but have the ideal hcp Fe lattice parameters which isolates the chemical contribution to the C_{ij} derivative. We verify the accuracy of Eq. (6) by directly calculating the total derivative of C_{ij} for selected solutes using a finite difference approximation similar to Eq. (16),

$$\left(\frac{\partial \widetilde{C_{ij}}}{\partial c_s}\right)_{\text{dir}} = N[C_{ij}^s(\Omega_{\text{eq}}) - C_{ij}^0]. \tag{17}$$

Eq. (17) differs from Eq. (16) since $C_{ij}^s(\Omega_{\text{eq}})$ is computed by straining supercells that contain a single solute and have fully relaxed lattice parameters. Hence, the directly calculated derivatives contain both the chemical and the strain contributions. The separate calculations of the strain and chemical contributions are more computationally efficient,

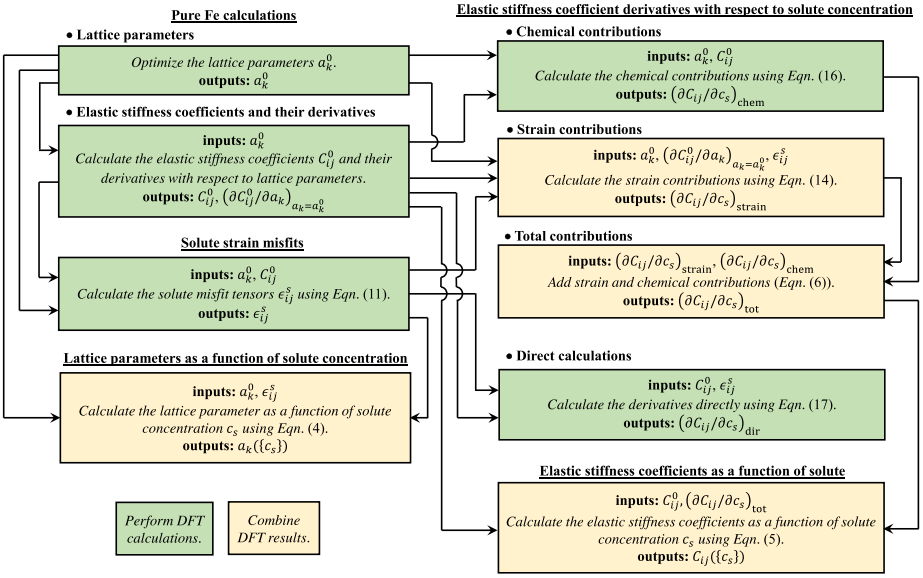

Fig. 1. Flowchart for computing the solute dependence of the hcp Fe lattice parameters a_k and elastic stiffness coefficients C_{ij}. The arrows show how the outputs from a given calculation serve as inputs to other calculations. The green boxes show steps requiring DFT calculations, and the tan boxes show steps that only use DFT results from previous steps to perform calculations.

however, since we compute the C_{ij}^0 derivatives in the strain contributions in Eq. (14) using two-atom hcp unit cells and the chemical contribution calculations in Eq. (16) require relaxing only atomic degrees of freedom. Fig. 1 outlines our computational approach for computing the solute-induced changes in the lattice parameters and C_{ij} in hcp Fe. The solute-dependent C_{ij} can also be used to compute the solute dependence of the polycrystalline bulk modulus B, shear modulus G, and Young's modulus E using the Voigt-Reuss-Hill averaging approach discussed in the Appendix.

We also examine the effect of solutes on the elastic anisotropy of hcp Fe under tension. The effective elastic compliance S' along the unit tensile direction $\mathbf{u}$ is [85]

$$S' = (1-u_3^2)^2 S_{11} + u_3^4 S_{33} + u_3^2(1-u_3^2)(2S_{13}+S_{44}), \tag{18}$$

where the S_{ij} are single-crystal elastic compliance coefficients written in contracted Voigt notation. Note that the only component of $\mathbf{u}$ that S' depends on is u_3 which corresponds to the a_3-axis (i.e., the c-axis) of the hcp crystal. We quantify the anisotropy under tensile loading as the ratio of the maximum value of S' with respect to u_3 to the minimum value of S'. This ratio changes with c_s through the solute dependence of the C_{ij} which determine the S_{ij}.

3. Computational results

Here we present the results of our DFT calculations of the lattice parameters and C_{ij} of ideal hcp Fe and hcp Fe with solutes. We compute the solute dependence of Voigt-Reuss-Hill (VRH) average polycrystalline elastic moduli using the equations given in the Appendix. We also compute the variation in the volumetric strain difference between hcp and bct Fe with solute concentration, and discuss how this effects the ε to α' transformation in steels. We compare our results to previous DFT-GGA calculations and available experimental data.

3.1. Properties of ideal hcp Fe

Table 2 lists our computed a_k^0 and C_{ij}^0 for pure Fe that enter into the solute-dependent lattice parameter model in Eq. (4) and C_{ij} model in Eq. (5), as well as the derivatives of the C_{ij}^0 with respect to a_k^0 that are inputs for the strain contributions to the solute dependence of the C_{ij} in Eq. (14). The table also shows that our results generally compare well with previous GGA calculations [60,61], with the C_{33}^0 and C_{44}^0 values from Ref. [60] showing the largest deviations from our results. We performed extensive tests using different k-point densities, energy smearing widths, plane-wave cutoff energies, and PAW potentials with different numbers of core electrons, and found deviations of less than 5% from our values in Table 2. These results combined with the good agreement

Table 2
Lattice parameters and elastic properties of pure hcp Fe at $T = 0$ K and $P = 0$ GPa. The second column gives our computed values and the third and fourth columns give results from previous DFT-GGA calculations. For hcp crystals, $C_{66}^0 = (C_{11}^0 - C_{12}^0)/2$. The a_k^0 and C_{ij}^0 values enter into Eqs. (4) and (5), and the $\partial C_{ij}^0/\partial a_k$ determine the strain contributions to $(\partial C_{ij}/\partial c_s)_{\text{tot}}$ given in Table 3. The anisotropy ratio $S'_{\max}/S'_{\min}$ is given by Eq. (18). Expressions for the Voigt-Reuss-Hill polycrystalline average Young's modulus E_{VRH}, shear modulus G_{VRH}, bulk modulus B_{VRH}, and Pugh's ratio $B_{\text{VRH}}/G_{\text{VRH}}$ are given in the Appendix.

	GGA, this study	GGA [60]	GGA [61]
a_1^0	2.459 Å	2.46	2.487
a_3^0	3.885	3.90	3.917
C_{11}^0	536 GPa	556	531.7
C_{33}^0	596	647	554.6
C_{12}^0	172	171	178.3
C_{13}^0	148	143	143.4
C_{44}^0	170	248	154.2
C_{66}^0	182	193	176.7
$\frac{\partial C_{11}^0}{\partial a_1}$, $\frac{\partial C_{11}^0}{\partial a_3}$	−2146, −234 GPa/Å	–	–
$\frac{\partial C_{33}^0}{\partial a_1}$, $\frac{\partial C_{33}^0}{\partial a_3}$	−1384, −880	–	–
$\frac{\partial C_{12}^0}{\partial a_1}$, $\frac{\partial C_{12}^0}{\partial a_3}$	−1033, −149	–	–
$\frac{\partial C_{13}^0}{\partial a_1}$, $\frac{\partial C_{13}^0}{\partial a_3}$	−524, −379	–	–
$\frac{\partial C_{44}^0}{\partial a_1}$, $\frac{\partial C_{44}^0}{\partial a_3}$	−293, −199	–	–
$\frac{\partial C_{66}^0}{\partial a_1}$, $\frac{\partial C_{66}^0}{\partial a_3}$	−556, −42	–	–
$S'_{\max}/S'_{\min}$	1.23	1.21	1.231
E_{VRH}	454 GPa	535	430.8
B_{VRH}	289	297	283.1
G_{VRH}	184	223	172.8
$B_{\text{VRH}}/G_{\text{VRH}}$	1.58	1.33	1.638

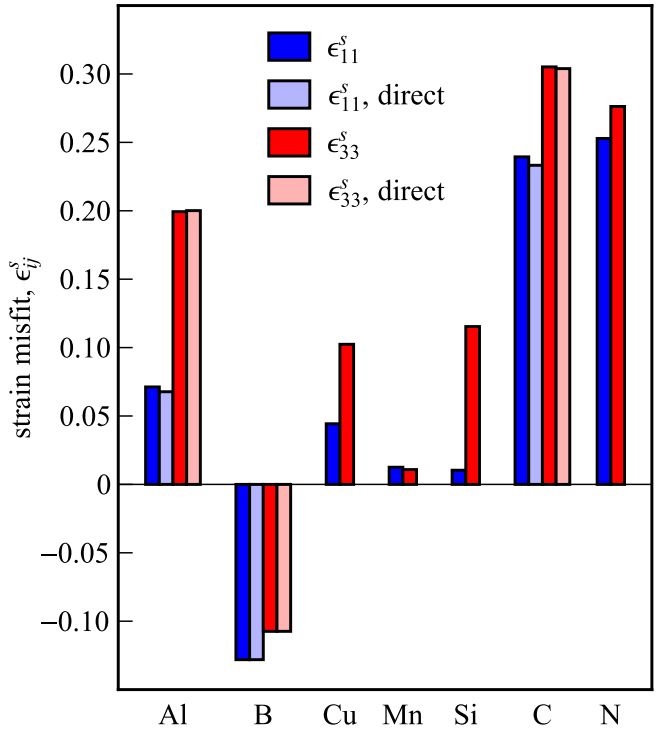

Fig. 2. Solute strain misfit tensor components ε^s_{ij} in hcp Fe. The calculations are performed using 4 × 4 × 3 supercells containing either one substitutional or one interstitial solute, corresponding to a solute concentration of ∼ 1.04 at.%. The dark bars show values computed from the solute-induced stress using Eq. (11). The light bars show values computed directly using Eq. (12) for Al, B, and C. The ε^s_{ij} computed using both methods agree closely for all three of these solutes. The data in the figure is for atomic concentration. For atomic percent, the values must be divided by 100.

between our values and the values from Ref. [61] suggest that the C^0_{33} and C^0_{44} values from Ref. [60] may be overpredicted. Our computed C^0_{ij} values satisfy the Born stability criteria for hcp crystals [86], which shows that non-magnetic hcp Fe is elastically stable at zero pressure. The table also lists the anisotropy ratio for single-crystal hcp Fe computed using Eq. (18), and the VRH estimates for the polycrystalline Young's modulus E_{VRH}, bulk modulus B_{VRH}, shear modulus G_{VRH}, and Pugh's ratio $B_{\mathrm{VRH}}/G_{\mathrm{VRH}}$ (see the Appendix for more details on the VRH moduli).

3.2. Effects of solutes on the hcp Fe a_k and C_{ij}

Fig. 2 shows the strain misfit tensor components for each solute computed from solute-induced stress, and verifies that the values agree with direct calculations for selected solutes. The strain misfit values for Al, Cu, Mn, Si, C, and N are positive which shows that these solutes are oversized in the hcp lattice, whereas the negative values for B show that it is undersized. Al has the largest effect among the substitutional solutes, whereas octahedral interstitial C and N have the largest overall effect. Mn has a small effect on the lattice parameters of hcp Fe, and corresponding small strain contributions to the solute derivatives of the C_{ij}. We compute strain misfit tensors for all of the solutes from the stress they induce in the lattice (see Eq. (11)), and we also compute strain misfit tensors directly (see Eq. (12)) for Al, B, and C. The close agreement between the two methods shows that the computationally efficient induced-stress method provides reliable strain misfit values. The strain misfit tensor components determine the derivatives of the a_k in Table 3, computed using Eqs. (8) and (11). The *ab initio* DLM study of hcp Fe-Mn random alloys in Ref. [51] computed the variation of the hcp lattice parameters a_k for Mn concentrations from 15 to 40 at.%, and Ref. [83] provides experimental measurements of a_k for Mn concentrations from ∼ 12 to 29 at.%. The variation of the DLM and experimental data is approximately linear over these full concentration ranges. We estimate that the slopes of a_1 and a_3 are ∼ +0.45 mÅ/at.% and ∼ +0.71 mÅ/at.% for DLM, and the experimental slopes reported in Ref. [83] are + 0.8886 mÅ/at.% and + 1.23 mÅ/at.%. Our computed slopes for a_1 and a_3 of + 0.31 mÅ/at.% and + 0.42 mÅ/at.% for Mn (see Table 3) agree well with the DLM values even though our calculations were performed at the much smaller Mn concentration of 1.04 at.%. This result suggests that Mn-Mn interactions are weak in hcp Fe, and that our linear model for the dependence of the lattice parameters on solute concentrations in Eq. (4) holds over a large concentration range for Mn. We also note that our calculations, the DLM calculations, and the experimental measurements show that Mn produces no change in a_3/a_1 from dilute concentrations (see Table 4) up to a concentration of 40 at.% (see Ref. [51]). Our computed a_k slopes for Mn and the DLM slopes are smaller than the experimental values, but all three sets of values indicate that Mn produces a small isotropic expansion of the hcp Fe lattice in contrast to the other solutes in this study.

Fig. 3 compares the strain (Eq. (14)) and chemical (Eq. (16)) contributions to the solute derivatives of the C_{ij} for hcp Fe, and shows that the sum of these separate contributions agrees with the more costly direct calculations (Eq. (17)) that encompass all of these effects. The close agreement between the two methods indicates that no higher-order derivatives are needed in Eq. (6) to accurately model the C_{ij} derivatives for dilute solute concentrations in hcp Fe. Mn has a small effect on all of the C_{ij} compared to the other solutes. We expect that the derivatives of the C_{ij} with respect to Mn concentration we computed for the dilute limit should provide a good estimate for the solute dependence at higher Mn concentration for two reasons. First, the strain contributions depend on the derivatives of the lattice parameters with respect to solute concentration (see Eq. (13)), and we showed in the last paragraph that the lattice parameter derivatives we computed for small Mn concentrations agree well with derivatives computed from DLM lattice parameter data for Mn concentrations up to 40 at.%. Second, the

Table 3
Derivatives of the lattice parameters a_k and elastic stiffness coefficients C_{ij} with respect to solute concentration c_s. The tabulated C_{ij} derivatives are the total values that consist of strain and chemical contributions (see Eq. (6)). The a_k derivatives determine the solute dependence of the hcp Fe lattice parameters in Eq. (4). The C_{ij} derivatives determine the solute dependence of the hcp Fe elastic stiffness coefficients in Eq. (5).

	$\frac{\partial a_1}{\partial c_s}\big\vert_{c_s=0}$	$\frac{\partial a_3}{\partial c_s}\big\vert_{c_s=0}$	$\left(\frac{\partial C_{11}}{\partial c_s}\right)_{\mathrm{tot}}$	$\left(\frac{\partial C_{33}}{\partial c_s}\right)_{\mathrm{tot}}$	$\left(\frac{\partial C_{12}}{\partial c_s}\right)_{\mathrm{tot}}$	$\left(\frac{\partial C_{13}}{\partial c_s}\right)_{\mathrm{tot}}$	$\left(\frac{\partial C_{44}}{\partial c_s}\right)_{\mathrm{tot}}$	$\left(\frac{\partial C_{66}}{\partial c_s}\right)_{\mathrm{tot}}$
Al	$+1.75\ \frac{\mathrm{mÅ}}{\mathrm{at.\%}}$	+7.75	$-12.19\ \frac{\mathrm{GPa}}{\mathrm{at.\%}}$	−8.83	+4.95	−1.80	−5.84	−8.57
B	−3.15	−4.18	−11.19	−5.12	+8.95	+2.67	−8.02	−10.07
Cu	+1.09	+3.98	−10.69	−7.90	+4.37	−0.42	−6.04	−7.53
Mn	+0.31	+0.42	−0.94	−0.31	+0.64	+0.04	+0.29	−0.79
Si	+0.26	+4.48	−8.22	−4.33	+5.52	−0.33	−4.75	−6.87
C	+5.89	+11.87	−10.94	−13.17	+4.59	+4.43	−5.12	−7.77
N	+6.22	+10.74	−11.76	−13.89	+4.92	+5.05	−5.86	−8.34

Table 4
Derivatives of a_3/a_1, the anisotropy ratio $S'_{\max}/S'_{\min}$, the Voigt-Reuss-Hill polycrystalline average Young's modulus E_{VRH}, shear modulus G_{VRH}, bulk modulus B_{VRH}, and Pugh's ratio $B_{\mathrm{VRH}}/G_{\mathrm{VRH}}$ with respect to solute concentration c_s. All of these derivatives are computed from the single-crystal derivatives listed in Table 3.

	$\frac{\partial}{\partial c_s}\left(\frac{a_3}{a_1}\right)\Big\vert_{c_s=0}$	$\frac{\partial}{\partial c_s}\left(\frac{S'_{\max}}{S'_{\min}}\right)\Big\vert_{c_s=0}$	$\frac{\partial E_{\mathrm{VRH}}}{\partial c_s}\Big\vert_{c_s=0}$	$\frac{\partial B_{\mathrm{VRH}}}{\partial c_s}\Big\vert_{c_s=0}$	$\frac{\partial G_{\mathrm{VRH}}}{\partial c_s}\Big\vert_{c_s=0}$	$\frac{\partial}{\partial c_s}\left(\frac{B_{\mathrm{VRH}}}{G_{\mathrm{VRH}}}\right)\Big\vert_{c_s=0}$
Al	$+0.0020\ (\mathrm{at.\%})^{-1}$	$+0.023$	$-14.14\ \frac{\mathrm{GPa}}{\mathrm{at.\%}}$	-3.37	-6.46	$+0.037\ (\mathrm{at.\%})^{-1}$
B	$+0.0003$	$+0.036$	-16.66	$+0.12$	-8.16	$+0.071$
Cu	$+0.0009$	$+0.022$	-13.37	-2.46	-6.21	$+0.040$
Mn	0.0000	-0.001	-0.47	-0.08	-0.22	$+0.001$
Si	$+0.0017$	$+0.023$	-10.75	-1.22	-5.09	$+0.037$
C	$+0.0010$	-0.005	-14.06	-0.90	-6.76	$+0.053$
N	$+0.0004$	-0.004	-15.42	-0.81	-7.43	$+0.059$

close agreement of the lattice parameter derivatives over such a large concentration range suggests that Mn-Mn interactions are weak and that the chemical contributions to the C_{ij} derivatives should also be fairly insensitive over a large range of Mn concentrations. Interstitial C and N produce the overall largest change in C_{33}. The total derivative values in Fig. 3 are listed in Table 3, and enter Eq. (5) to give the solute dependence of the C_{ij}. The derivatives of the single-crystal C_{ij} determine the derivatives of the anisotropy ratio S'_{max}/S'_{min} and VRH polycrystalline moduli listed in Table 4. None of the solutes has a strong impact on the elastic anisotropy $S'_{\max}/S_{\min}$ or the Pugh's ratio $B_{\mathrm{VRH}}/G_{\mathrm{VRH}}$ of hcp Fe.

Fig. 4 shows the variation of the polycrystalline shear modulus G_{VRH} and Young's modulus E_{VRH} with solute concentration. Manganese has a small effect on E_{VRH} and G_{VRH}, whereas B has the largest effect.

In summary, Eq. (4) gives the hcp Fe lattice parameters a_k as functions of solute concentration and Eq. (5) gives the single-crystal C_{ij} as functions of solute concentration. The derivatives with respect to solute concentration that enter these models are given in Table 3. Similar linear models can be used to compute the dilute-limit solute dependence of quantities derived from the single-crystal a_k and C_{ij}, including a_3/a_1, $S'_{\max}/S'_{\min}$, E_{VRH}, B_{VRH}, G_{VRH}, and $B_{\mathrm{VRH}}/G_{\mathrm{VRH}}$. The

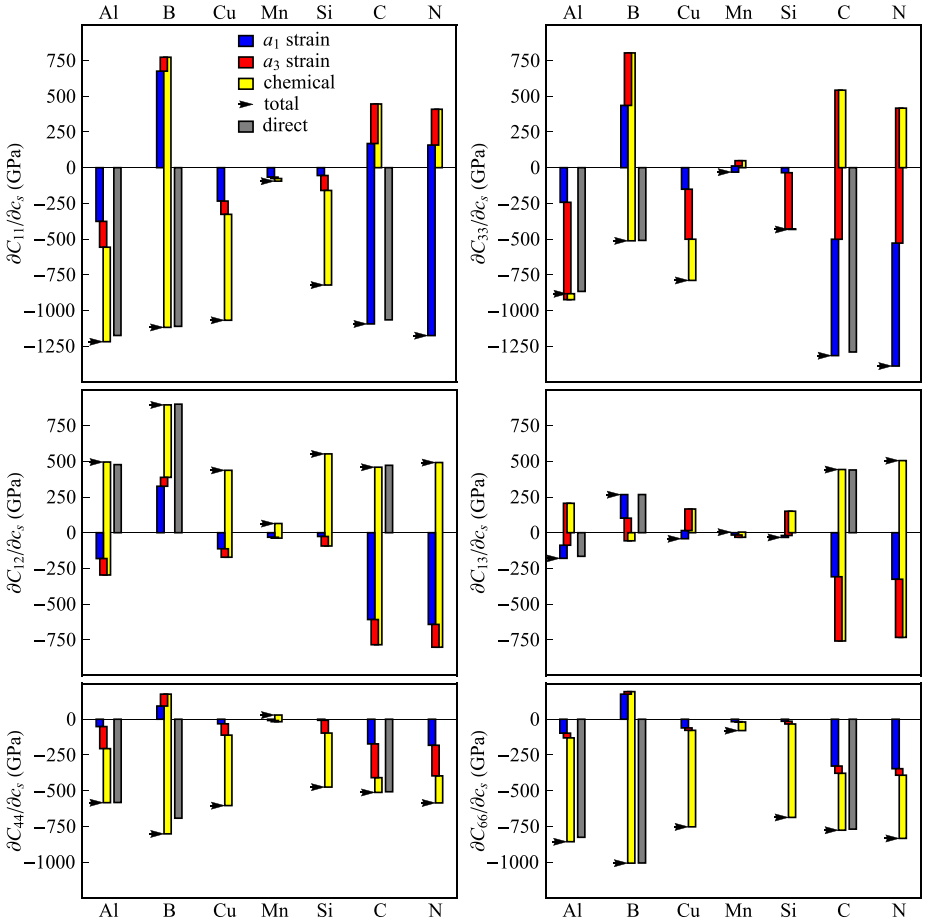

Fig. 3. Derivatives of the hcp Fe C_{ij} with respect to solute concentration. The calculations are performed using $4 \times 4 \times 3$ supercells containing either one substitutional or one interstitial solute, corresponding to a solute concentration of ~ 1.04 at.%. The C_{ij} derivatives consist of three contributions: two strain contributions due to the changes in a_1 (blue) and a_3 (red), and one contribution from the local change in chemical bonding around the solute (yellow). When the derivative contributions have the same sign the bars are stacked on each other. When necessary, the bars are shifted vertically so that the total positive contributions and the total negative contributions overlap to display the partial cancellation of the different terms. The total derivative values given by the sum of all three contributions are indicated by the arrows. In the cases of Al, B, and C, we also compute the C_{ij} derivatives directly (gray) by applying strains to supercells that contain a solute and have fully relaxed lattice parameters. The direct calculations closely match the sum of the strain and chemical contributions for all three of these solutes.

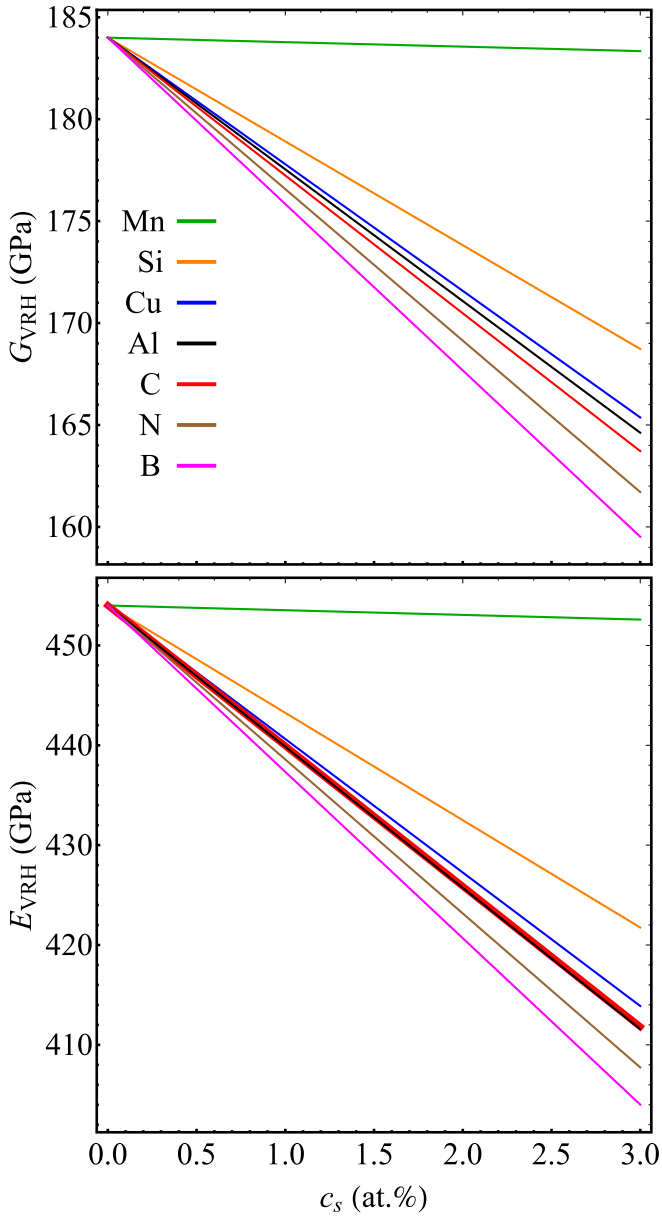

Fig. 4. Voigt-Reuss-Hill average polycrystalline shear modulus G_{VRH} and Young's modulus E_{VRH} vs. solute concentration. All of the solutes reduce both moduli. Mn produces the smallest changes in the moduli, whereas B has the largest effect. For a given solute concentration, the change in E_{VRH} is larger than the change in G_{VRH} for each solute (see Table 4 for the values of the derivatives).

appropriate solute derivatives for these quantities are listed in Table 4.

3.3. Implications for the ε to α′ transformation

The driving force for martensitic transformations is the free energy difference between the parent and product phases, which contains a strain energy contribution [4,47,48,87,88] arising from the lattice parameter mismatch between the phases. The strain is accommodated by plastic deformation in the ε to α′ transformation [3], and the associated strain energy increases with the density of dislocations generated by the transformation [87,89]. The dislocation density in martensite depends on several factors including alloy chemistry and temperature [90–93], but correlates well with the volumetric strain associated with the transformation from austenite to martensite in Fe-C and Fe-Ni alloys [92]. We therefore estimate the effect of solutes on the volumetric

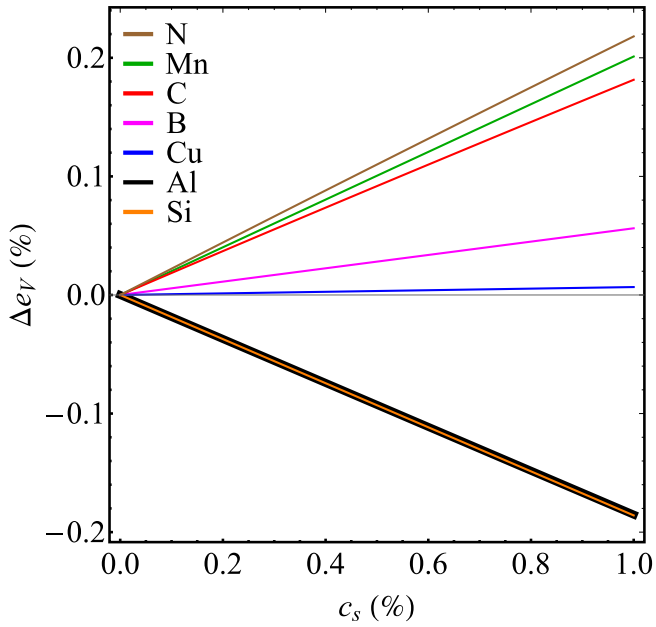

Fig. 5. Change in volumetric strain e_V between hcp Fe and bct Fe versus solute concentration c_s. In the absence of solutes, e_V is positive. An increase in e_V with c_s therefore aids in stabilizing the ε phase against transformation to the α′ phase since it will increase the strain energy between the phases. N, Mn, and C provide the largest stabilizing effect, whereas the decrease in e_V due to Al and Si should promote the transformation of the ε phase to the α′ phase.

strain e_V between the α′ and ε phases using the solute dependence of the lattice parameters a_k for hcp and bct Fe. The solute dependence of these quantities for hcp Fe is given in Table 3, and for bct Fe we use the values we computed in Ref. [53]. The volumetric strain is [48,82,88]

$$e_V = \frac{V^{\mathrm{m}}_{\mathrm{bct}} - V^{\mathrm{m}}_{\mathrm{hcp}}}{V^{\mathrm{m}}_{\mathrm{hcp}}}, \tag{19}$$

where

$$V^{\mathrm{m}}_{\mathrm{hcp}} = \frac{\sqrt{3}}{4} a^2_{1,\mathrm{hcp}} a_{3,\mathrm{hcp}} N_{\mathrm{A}}, \tag{20}$$

$$V^{\mathrm{m}}_{\mathrm{bct}} = \frac{1}{2} a^2_{1,\mathrm{bct}} a_{3,\mathrm{bct}} N_{\mathrm{A}}. \tag{21}$$

Fig. 5 shows the change in e_V versus solute concentration c_s. The solute-free value of e_V is positive, so an increase in e_V aids in stabilizing the ε phase against transformation to the α′ phase by increasing the strain energy associated with the transformation. Our DFT calculations show that N, Mn, and C have the largest stabilizing effect, whereas Si and Al will promote the transformation to the α′ phase. Our DFT-computed lattice parameter derivatives for Mn in bct Fe [52,53] are ∼ 2 to 3 times larger than experimentally measured values [81,82] which may reduce the slope of e_V by up to a factor of ∼ 5, but the increase in strain energy due to Mn should still have a stabilizing effect on the ε phase especially in high-Mn steels.

4. Summary and discussion

We present DFT calculations of solute-induced changes in the lattice parameters a_k and single-crystal C_{ij} of non-magnetic hcp Fe due to dilute concentrations of Al, B, C, Cu, Mn, Si, C, and N solutes. We treat Al, Cu, Mn, and Si as substitutional solutes. Our formation energy calculations show that B is most energetically stable as a substitutional solute, whereas C and N are most energetically stable as octahedral interstitial solutes in hcp Fe. We compute strain misfit tensors that determine the solute dependence of the a_k, and we compute the strain and chemical

contributions to the derivatives of the single-crystal elastic constants C_{ij} with respect to solute concentration. Our direct calculations of the derivatives of the a_k and C_{ij} show that the more computationally efficient strain misfit and chemical contribution calculations provide consistent solute derivative values. These results confirm that the approach we developed for bcc [52] and bct [53] Fe applies equally well to hcp Fe. We find that Mn produces a much smaller effect on the lattice parameters and C_{ij} of hcp Fe than the other solutes. Our derivatives of the lattice parameters with respect to solute concentration are strictly valid in the dilute limit, but the close agreement between our Mn values and values computed from literature data for Mn concentrations between 15 and 40 at.% suggest that our data can be used to model the lattice parameters of ε-martensite in multi-phase medium- to high-Mn structural steels. This result also suggests that Mn-Mn interactions are weak in hcp Fe and that our computed C_{ij} derivatives with respect to Mn concentration can be used to estimate the elastic properties of the ε-martensite phase in steels with large concentrations of Mn. Further studies could investigate this idea using computational supercells with larger Mn concentrations than we considered, for example special quasi-random structures to model concentrated random Fe-Mn alloys. Our computed solute-dependent lattice parameters and C_{ij} can also be used as inputs for microstructure-based models of multiphase steels containing the ε-martensite phase, allowing the study of alloy composition on elastic and plastic response [46,54].

We use our computed a_k and C_{ij} derivatives to estimate solute effects on the polycrystalline elastic moduli and strain energies associated with martensitic transformations. We compute the solute dependence of the polycrystalline Young's and shear moduli of hcp Fe within the Voigt-Reuss-Hill approximation. We find that Mn has a weak effect on the polycrystalline moduli and B has the strongest effect. Additionally, we show that C, Mn, and N solutes should increase the volumetric strain difference associated with the ε to α′ phase transformation in steels. Accordingly, these solutes should help to stabilize the ε phase against transformation to α′ by increasing the strain energy difference between the two phases. Conversely, Al and Si solutes lower the strain energy which promotes the transformation to the α′ phase. Our strain data can be combined with data on chemical and interfacial contributions to the total transformation free energies to model martensitic transformations in multiphase steels containing ε-martensite.

Data availability

The raw and processed data required to reproduce these findings are available to download from http://hdl.handle.net/11256/982.

CRediT authorship contribution statement

Michael R. Fellinger: Conceptualization, Methodology, Investigation, Formal analysis, Visualization, Writing - original draft, Writing - review & editing. **Louis G. Hector Jr:** Conceptualization, Investigation, Resources, Supervision, Project administration, Writing - review & editing. **Dallas R. Trinkle:** Funding acquisition, Supervision, Writing - review & editing.

Acknowledgements

This material is based upon work supported by the Department of Energy National Energy Technology Laboratory under Award Number (s) DE-EE0005976. This report was prepared as an account of work sponsored by an agency of the United States Government. Neither the United States Government nor any agency thereof, nor any of their employees, makes any warranty, express or implied, or assumes any legal liability or responsibility for the accuracy, completeness, or usefulness of any information, apparatus, product, or process disclosed, or represents that its use would not infringe privately owned rights. Reference herein to any specific commercial product, process, or service by trade name, trademark, manufacturer, or otherwise does not necessarily constitute or imply its endorsement, recommendation, or favoring by the United States Government or any agency thereof. The views and opinions of authors expressed herein do not necessarily state or reflect those of the United States Government or any agency thereof. The research was performed using computational resources sponsored by the Department of Energy's Office of Energy Efficiency and Renewable Energy and located at the National Renewable Energy Laboratory. Additional computational resources were provided by the National Energy Research Scientific Computing Center, the General Motors High Performance Computing Center, and the Taub cluster maintained and operated by the Computational Science and Engineering Program at the University of Illinois.

Appendix A. Polycrystalline elastic moduli

The bulk modulus B, shear modulus G, and Young's modulus E of an isotropic polycrystalline sample comprised of grains with hexagonal symmetry can be estimated from the single-crystal elastic stiffness coefficients C_{ij} using the Voigt, Reuss, or Voigt-Reuss-Hill averaging procedures [45,94,95]. The Voigt and Reuss averages present upper and lower bounds on the polycrystalline moduli, respectively, and the Voigt-Reuss-Hill moduli are the arithmetic means of the Voigt and Reuss values. The Voigt (V) averages of the moduli are

$$B_{\mathrm{V}} = \frac{2C_{11} + C_{33} + 2C_{12} + 4C_{13}}{9}, \tag{A.1}$$

$$G_{\mathrm{V}} = \frac{12C_{44} + 12C_{66} + M}{30}, \tag{A.2}$$

$$E_{\mathrm{V}} = \frac{9B_{\mathrm{V}}G_{\mathrm{V}}}{3B_{\mathrm{V}} + G_{\mathrm{V}}}, \tag{A.3}$$

where $C_{66} = (C_{11} - C_{12})/2$ and the auxiliary modulus $M = C_{11} + 2C_{33} + C_{12} - 4C_{13}$ [94]. The Reuss (R) averages of the moduli are

$$B_{\mathrm{R}} = \frac{C^2}{M}, \tag{A.4}$$

$$G_{\mathrm{R}} = \frac{5}{2}\left[\frac{C_{44}C_{66}C^2}{(C_{44} + C_{66})C^2 + 3B_{\mathrm{V}}C_{44}C_{66}}\right] \tag{A.5}$$

$$E_{\mathrm{R}} = \frac{9B_{\mathrm{R}}G_{\mathrm{R}}}{3B_{\mathrm{R}} + G_{\mathrm{R}}}, \tag{A.6}$$

where the auxiliary modulus $C^2 = (C_{11} + C_{12})C_{33} - 2C_{13}^2$ [94]. The Voigt-Reuss-Hill (VRH) values for the moduli are

$$B_{\mathrm{VRH}} = \frac{B_{\mathrm{V}} + B_{\mathrm{R}}}{2}, \tag{A.7}$$

$$G_{\mathrm{VRH}} = \frac{G_{\mathrm{V}} + G_{\mathrm{R}}}{2}, \tag{A.8}$$

$$E_{\mathrm{VRH}} = \frac{9B_{\mathrm{VRH}}G_{\mathrm{VRH}}}{3B_{\mathrm{VRH}} + G_{\mathrm{VRH}}}. \tag{A.9}$$

Pugh's ratio $B_{\mathrm{VRH}}/G_{\mathrm{VRH}}$ is a measure of ductility [96,97], with values greater than ~ 1.75 indicating ductile behavior and lower values indicating brittle behavior.

The derivatives of the single-crystal C_{ij} with respect to solute concentration determine the derivatives of the polycrystalline elastic moduli. The derivatives of B_{V}, G_{V}, and E_{V} with respect to solute concentration are

$$\frac{\partial B_{\mathrm{V}}}{\partial c_s} = \frac{2}{9}\frac{\partial C_{11}}{\partial c_s} + \frac{1}{9}\frac{\partial C_{33}}{\partial c_s} + \frac{2}{9}\frac{\partial C_{12}}{\partial c_s} + \frac{4}{9}\frac{\partial C_{13}}{\partial c_s}, \tag{A.10}$$

$$\frac{\partial G_{\mathrm{V}}}{\partial c_s} = \frac{2}{5}\frac{\partial C_{44}}{\partial c_s} + \frac{2}{5}\frac{\partial C_{66}}{\partial c_s} + \frac{1}{30}\frac{\partial M}{\partial c_s}, \tag{A.11}$$

$$\frac{\partial E_{\mathrm{V}}}{\partial c_s} = (3B_{\mathrm{V}} + G_{\mathrm{V}})^{-2}\left(9G_{\mathrm{V}}^2\frac{\partial B_{\mathrm{V}}}{\partial c_s} + 27B_{\mathrm{V}}^2\frac{\partial G_{\mathrm{V}}}{\partial c_s}\right), \tag{A.12}$$

where the derivative of M is

$$\frac{\partial M}{\partial c_s} = \frac{\partial C_{11}}{\partial c_s} + 2\frac{\partial C_{33}}{\partial c_s} + \frac{\partial C_{12}}{\partial c_s} - 4\frac{\partial C_{13}}{\partial c_s}. \tag{A.13}$$

The derivatives of B_{R}, G_{R}, and E_{R} with respect to solute concentration are

$$\frac{\partial B_{\mathrm{R}}}{\partial c_s} = \frac{1}{M}\frac{\partial (C^2)}{\partial c_s} - \frac{C^2}{M^2}\frac{\partial M}{\partial c_s}, \tag{A.14}$$

$$\frac{\partial G_{\mathrm{R}}}{\partial c_s} = \frac{5C^2}{2}\left[\left(C_{44}^2\frac{\partial C_{66}}{\partial c_s} + C_{66}^2\frac{\partial C_{44}}{\partial c_s}\right)C^2 - 3C_{44}^2C_{66}^2\frac{\partial B_{\mathrm{V}}}{\partial c_s} - C_{44}C_{66}\left(C_{44} + C_{66}\right)\frac{\partial (C^2)}{\partial c_s}\right]\cdot[3C_{44}C_{66}B_{\mathrm{V}} + (C_{44} + C_{66})C^2]^{-2}, \tag{A.15}$$

$$\frac{\partial E_{\mathrm{R}}}{\partial c_s} = (3B_{\mathrm{R}} + G_{\mathrm{R}})^{-2}\left(9G_{\mathrm{R}}^2\frac{\partial B_{\mathrm{R}}}{\partial c_s} + 27B_{\mathrm{R}}^2\frac{\partial G_{\mathrm{R}}}{\partial c_s}\right), \tag{A.16}$$

where the derivative of C^2 is

$$\frac{\partial (C^2)}{\partial c_s} = C_{33}\left(\frac{\partial C_{11}}{\partial c_s} + \frac{\partial C_{12}}{\partial c_s}\right) + \left(C_{11} + C_{12}\right)\frac{\partial C_{33}}{\partial c_s} - 4C_{13}\frac{\partial C_{13}}{\partial c_s}. \tag{A.17}$$

The derivatives of B_{VRH} and G_{VRH} are averages of the V and R derivatives. The derivatives of E_{VRH} are given by expressions similar to the V and R expressions, with the V or R moduli replaced by the VRH moduli. Table 4 gives the DFT-computed values of the VRH polycrystalline moduli derivatives.

References

[1] W.C. Leslie, The Physical Metallurgy of Steels, Techbooks, Herndon, 1991.
[2] H. Berns, W. Theisen, Ferrous Materials: Steel and Cast Iron, Springer-Verlag, Berlin, 2008.
[3] G.B. Olson, M. Cohen, A mechanism for the strain-induced nucleation of martensitic transformations, J. Less-Comm. Metals 28 (1972) 107–118.
[4] G.B. Olson, M. Cohen, A general mechanism of martensitic nucleation: Part I. General concepts and the FCC →HCP transformation, Metall. Trans. A 7A (1976) 1897–1904.
[5] G.B. Olson, M. Cohen, A general mechanism of martensitic nucleation: Part II. FCC →BCC and other martensitic transformations, Metall. Trans. A 7A (1976) 1905–1914.
[6] G.B. Olson, M. Cohen, A perspective on martensitic nucleation, Ann. Rev. Mater. Sci. 11 (1981) 1–30.
[7] Y.F. Shen, X.X. Li, X. Sun, Y.D. Wang, L. Zuo, Twinning and martensite in a 304 austenitic stainless steel, Mat. Sci. Eng. A 552 (2012) 514–522.
[8] F. Abu-Farha, X. Hu, X. Sun, Y. Ren, L.G. Hector Jr., G. Thomas, T.W. Brown, In Situ local measurement of austenite mechanical stability and transformation behavior in third-generation advanced high-strength steels, Met. Mat. Trans. A 49A (2018) 2583–2596.
[9] M. Hatano, Y. Kubota, T. Shobu, S. Mori, Presence of ϵ-martensite as an intermediate phase during the strain-induced transformation of SUS304 stainless steel, Philos. Mag. Lett. 96 (2016) 220–227.
[10] K. Ishida, T. Nishizawa, Effect of alloying elements on stability of epsilon iron, Trans. JIM 15 (1974) 225–231.
[11] M. Acet, T. Schneider, B. Gehrmann, E. Wassermann, The magnetic aspects of the γ-α and γ-ε martensitic transformations in Fe-Mn alloys, J. Physique IV 5 (1995) C8-379-C8-384.
[12] J.H. Jang, J. Moon, H.-Y. Ha, T.-H. Lee, D.-W. Suh, Quantum-mechanical analysis of effect of alloying elements on ϵ-martensite start temperature of steels, Sci. Rep. 7 (2017) 17860.
[13] J.A. Venables, The martensite transformation in stainless steel, Philos. Mag. 7 (1962) 35–44.
[14] A. Sato, K. Soma, T. Mori, Hardening due to pre-existing ε –martensite in an Fe-30Mn-1Si alloy single crystal, Acta Metall. 30 (1982) 1901–1907.
[15] X.-S. Yang, S. Sun, X.-L. Wu, E. Ma, T.-Y. Zhang, Dissecting the mechanism of martensitic transformation via atomic-scale observations, Sci. Rep. 4 (2014) 6141.
[16] X.-S. Yang, S. Sun, T.-Y. Zhang, The mechanism of bcc α′ nucleation in single hcp ε laths in the fcc γ→hcp ε→ bcc α′ martensitic phase transformation, Acta Mater. 95 (2015) 264–273.
[17] X.-S. Yang, S. Sun, H.H.R.S.-Q. Shi, T.-Y. Zhang, Shear and shuffling accomplishing polymorphic fcc γ→ hcp ε→ bct α martensitic phase transformation, Acta Mater. 136 (2017) 347–354.
[18] O. Grässel, L. Krüger, G. Frommeyer, L.W. Meyer, High strength Fe-Mn-(Al, Si) TRIP/TWIP steels development — properties — application, Int. J. Plast. 16 (2000) 1391–1409.
[19] R.B. Figueiredo, F.L. Sicupira, L.R.C. Malheiros, M. Kawasaki, D.B. Santos, T.G. Langdon, Formation of epsilon martensite by high-pressure torsion in a TRIP steel, Mater. Sci. Eng. A 625 (2015) 114–118.
[20] E.I. Galindo-Nava, P.E.J. Rivera-Díaz-del-Castillo, Understanding martensite and twin formation in austenitic steels: a model describing TRIP and TWIP effects, Acta Mater. 128 (2017) 120–134.
[21] R. Alturk, L.G. Hector Jr., C.M. Enloe, F. Abu-Farha, T.W. Brown, Strain rate effect on tensile flow behavior and anisotropy of a medium-manganese TRIP steel, JOM 70 (2018) 894–905.
[22] K. Yan, D. Bhattacharyya, Q. Lian, S. Kabra, M. Kawasaki, D.G. Carr,

M.D. Callaghan, M. Avdeev, H. Li, Y. Wang, X. Liao, T.G. Langdon, K. Liss, R.J. Dippenaar, Martensitic phase transformation and deformation behavior of Fe-Mn-C-Al twinning-induced plasticity steel during high-pressure torsion, Adv. Eng. Mater. 17 (2014) 927–932.
[23] J. Dash, H.M. Otte, The martensite transformation in stainless steel, Acta Metall. 11 (1963) 1169–1178.
[24] P.L. Mangonon, G. Thomas, The martensite phases in 304 stainless steel, Metall. Trans. 1 (1970) 1577–1586.
[25] H. Fujita, S. Ueda, Stacking faults and F.C.C. (γ)→H.C.P. (ε) transformation in 18/8-type stainless steel, Acta Metall. 20 (1972) 759–767.
[26] C.X. Huang, G. Yang, B. Deng, S.D. Wu, S.X. Li, Z.F. Zhang, Formation mechanism of nanostructures in austenitic stainless steel during equal channel angular pressing, Philos. Mag. 87 (2007) 4949–4971.
[27] S. Scheriau, Z. Zhang, S. Kleber, R. Pippan, Deformation mechanisms of a modified 316L austenitic steel subjected to high pressure torsion, Mat. Sci. Eng. A 528 (2011) 2776–2786.
[28] A. Sato, E. Chishima, K. Soma, T. Mori, Shape memory effect in $\gamma \rightleftharpoons \varepsilon$ transformation in Fe-30Mn-1Si alloy single crystals, Acta Metall. 30 (1982) 1177–1983.
[29] A. Sato, E. Chishima, K. Soma, T. Mori, Physical properties controlling shape memory effect in Fe-Mn-Si alloys, Acta Metall. 34 (1986) 287–294.
[30] M. Murakami, H. Otsuka, H.G. Suzuki, S. Matsuda, Complete shape memory effect in polycrystalline Fe-Mn-Si alloys, in: Proceedings of the International Conference on Martensitic transformations, Japan Inst. Met. ICOMAT-86 (1986) 985–990.
[31] H. Otsuka, H. Yamada, T. Maruyama, H. Tanahashi, S. Matsuda, M. Murakami, Effects of alloying additions on Fe-Mn-Si shape memory alloys, Trans. ISIJ 30 (1990) 674–679.
[32] Y. Moriya, M. Suzuki, S. Hashizume, T. Sampei, I. Kozasu, Effect of alloying elements on shape memory effect, Proc. ICSS (1991) 527–532.
[33] T. Kikuchi, S. Kajiwara, Y. Tomota, Microscopic studies on stress-induced martensite-transformation and its reversion in an Fe-Mn-Si-Cr-Ni shape-memory alloy, Mater. Trans. 36 (1995) 719–728.
[34] Y.H. Wen, M. Yan, N. Li, Effects of carbon addition and aging on the shape memory effect of Fe-Mn-Si-Cr-Ni alloys, Scr. Mater. 50 (2004) 441–444.
[35] V.V. Bliznuk, V.G. Gavriljuk, G.P. Kopitsa, S.V. Grigoriev, V.V. Runov, Fluctuations of chemical composition of austenite and their consequence on shape memory effect in Fe-Mn-(Si, Cr, Ni, C, N) alloys, Acta Mater. 52 (2004) 4791–4799.
[36] N. Van Caenegem, L. Duprez, K. Verbeken, B.C.D. Cooman, Y. Houbaert, D. Segers, Effect of carbon on the shape memory effect in FeMnSiCrNi SMAs, ISIJ 47 (2007) 723–732.
[37] K. Verbeken, N. Van Caenegem, D. Raabe, Identification of ε martensite in a Fe-based shape memory alloy by means of EBSD, Micron 40 (2009) 151–156.
[38] C. Leinenbach, A. Arabi-Hashemia, W.J. Lee, A. Lis, M. Sadegh-Ahmadi, S.V. Petegem, T. Panzner, H.V. Swygenhoven, Characterization of the deformation and phase transformation behavior of VC-free and VC-containing FeMnSi-based shape memory alloys by in situ neutron diffraction, Mater. Sci. Eng. A 703 (2017) 314–323.
[39] R. Lagneborg, The martensite transformation in 18% Cr-8% Ni steels, Acta Metall. 12 (1964) 823–843.
[40] P.M. Kelly, The martensite transformation in steels with low stacking fault energy, Acta Metall. 13 (1965) 635–646.
[41] P.C. Maxwell, A. Goldberg, J.C. Shyne, Stress-assisted and strain-induced martensites in Fe-Ni-C alloys, Metall. Trans. 5 (1974) 1305–1318.
[42] L. Bracke, L. Kestens, J. Penning, Transformation mechanism of α′-martensite in an austenitic Fe-Mn-C-N alloy, Scr. Mat. 57 (2007) 385–388.
[43] X. Wang, W. Lui, D. Embury, Morphology and distribution of martensite in 301L alloy induced by different subsequent processes after prior deformation, Can. Metall. Q. 50 (2011) 396–407.
[44] W. Zhang, Z. Liu, Z. Zhang, G. Wang, The crystallographic mechanism for deformation induced martensitic transformation observed by high resolution transmission electron microscope, Mater. Lett. 91 (2013) 158–160.
[45] G. Grimvall, Thermophysical Properties of Materials, second ed., North Holland, 1999.
[46] F. Pourboghrat, A.-F. Fadi, H. Kim, L.G. Hector Jr., M.R. Fellinger, R. Esameilpour, T.P.X. Hu, Crystal plasticity modeling of third generation multi-phase AHSS with martensitic transformation, Int. J. Plast. (2019) (in press).
[47] D.A. Porter, K.E. Easterling, Phase Transformations in Metals and Alloys, second ed., Nelson Thornes, 1992.
[48] D.T. Pierce, J.A. Jiménez, J. Bentley, D. Raabe, C. Oskay, J.E. Wittig, The influence of manganese content on the stacking fault and austenite/ε-martensite interfacial energies in Fe-Mn-(Al-Si) steels investigated by experiment and theory, Acta Mater. 68 (2014) 238–253.
[49] G.R. Speich, A.J. Schwoeble, W.C. Leslie, Elastic constants of binary iron-base alloys, Metall. Trans. 3 (1972) 2031–2037.
[50] H. Zhang, M.P.J. Punkkinen, B. Johansson, S. Hertzman, L. Vitos, Single-crystal elastic constants of ferromagnetic bcc Fe-based random alloys from first-principles theory, Phys. Rev. B 81 (2010) 184105.
[51] T. Gebhardt, D. Music, B. Hallstedt, M. Ekholm, I.A. Abrikosov, L. Vitos, J.M. Schneider, *Ab initio* lattice stability of fcc and hcp Fe-Mn random alloys, J. Phys.: Condens. Matter 22 (2010) 295402.
[52] M.R. Fellinger, L.G. Hector Jr., D.R. Trinkle, Ab initio calculations of the lattice parameter and elastic stiffness coefficients of bcc Fe with solutes, Comput. Mater. Sci. 126 (2017) 503–513.
[53] M.R. Fellinger, L.G. Hector Jr., D.R. Trinkle, Effect of solutes on the lattice parameters and elastic stiffness coefficients of body-centered tetragonal Fe, Comput. Mat. Sci. 152 (2018) 308–323.
[54] M. Friák, W.A. Counts, D. Ma, B. Sander, D. Holec, D. Raabe, J. Neugebauer, Theory-guided materials design of multi-phase Ti-Nb alloys with bone-matching elastic properties, Materials 5 (2012) 1853–1872.
[55] F. Roters, P. Eisenlohr, L. Hantcherli, D.D. Tjahjanto, T.R. Bieler, D. Raabe, Overview of constitutive laws, kinematics, homogenization and multiscale methods in crystal plasticity finite-element modeling: theory, experiments, applications, Acta Mater. 58 (2010) 1152–1211.
[56] S.A. Kim, W.L. Johnson, Elastic constants and internal friction of martensitic steel, ferritic-pearlitic steel, and α-iron, Mater. Sci. Eng. A 452–453 (2017) 633–639.
[57] L. Cheng, A. Böttger, T.H. de Keijser, E.J. Mittemeijer, Lattice parameters of iron-carbon and iron-nitrogen martensites and austenites, Scr. Metal. Mater. 24 (1990) 509–514.
[58] M. Souissi, H. Numakura, Elastic properties of Fe-C and Fe-N martensites, ISIJ Int. 55 (2015) 1512–1521.
[59] G. Steinle-Neumann, L. Stixrude, R.E. Cohen, First-principles elastic constants for the hcp transition metals Fe Co, and Re at high pressure, Phys. Rev. B 60 (1999) 791–799.
[60] G.Y. Guo, H.H. Wang, Gradient-corrected density functional calculation of elastic constants of Fe, Co and Ni in bcc, fcc, and hcp structures, Chin. J. Phys. 38 (2000) 949–961.
[61] S.L. Qiu, P.M. Marcus, Elasticity of hcp nonmagnetic Fe under pressure, Phys. Rev. B 68 (2003) 054103.
[62] L. Vočadlo, D.P. Dobson, I.G. Wood, *Ab initio* calculations of the elasticity of hcp-Fe as a function of temperature at inner-core pressure, Earth Planet. Sci. Lett. 288 (2009) 534–538.
[63] T. Tsuchiya, M. Fujibuchi, Effects of Si on the elastic property of Fe at Earth's inner core pressures: First principles study, Phys. Earth Planet. Int. 174 (2009) 212–219.
[64] B. Martorell, I.G. Wood, J. Brodholt, L. Vočadlo, The elastic properties of hcp-$Fe_{1-x}Si_x$ at Earth's inner-core conditions, Earth Planet. Sci. Lett. 451 (2016) 89–96.
[65] Y. Li, L. Vočadlo, J.P. Brodholt, The elastic properties of *hcp*-Fe alloys under the conditions of the Earth's inner core, Earth Planet. Sci. Lett. 493 (2018) 118–127.
[66] G. Kresse, J. Furthmüller, Efficient iterative schemes for ab initio total-energy calculations using a plane-wave basis set, Phys. Rev. B 54 (1996) 11169–11186.
[67] J.P. Perdew, K. Burke, M. Ernzerhof, Generalized gradient approximation made simple, Phys. Rev. Lett. 77 (1996) 3865–3868.
[68] P.E. Blöchl, Projector augmented-wave method, Phys. Rev. B 50 (1994) 17953–17979.
[69] G. Kresse, D. Joubert, From ultrasoft pseudopotentials to the projector augmented-wave method, Phys. Rev. B 59 (1999) 1758–1775.
[70] M. Methfessel, A.T. Paxton, High-precision sampling for Brillouin-zone integration in metals, Phys. Rev. B 40 (1989) 3616–3621.
[71] P.E. Blöchl, O. Jepsen, O.K. Andersen, Improved tetrahedron method for Brillouin-zone integrations, Phys. Rev. B 49 (1994) 16223–16233.
[72] D.R. Trinkle, Lattice and elastic constants of titanium-niobium monoborides containing aluminum and vanadium, Scr. Mater. 56 (2007) 273–276.
[73] H. Kim, D.R. Trinkle, Mechanical properties and phase stability of monoborides using density functional theory calculations, Phys. Rev. Mater. 1 (2017) 013601.
[74] R.A. Johnson, Internal relaxation in the HCP lattice, Modell. Simul. Mat. Sci. Eng. 1 (1993) 717–722.
[75] F. Jona, P.M. Marcus, Hexagonal and tetragonal states of magnesium by first principles, Phys. Rev. B 66 (2002) 094104.
[76] B. Fornberg, Generation of finite difference formulas on arbitrarily spaced grids, Math. Comput. 51 (1988) 699–706.
[77] J. Jung, M. Fricke, G. Hampel, J. Hesse, ^{57}Fe Mössbauer effect studies on the magnetism of iron-rich bcc, fcc, and hcp phases of $Fe_{100-c}Mn_c$, Hyperfine Interact. 72 (1992) 375–388.
[78] T. Hinomura, S. Nasu, Y. Tomota, ^{57}Fe Mössbauer study of γ-FeMn and ε-FeMn alloys, J. Japan. Inst. Met. 62 (1998) 635–641.
[79] H.H. Wu, P. Wisesa, D.R. Trinkle, Oxygen diffusion in hcp metals from first principles, Phys. Rev. B 94 (2016) 014307.
[80] R. Agarwal, D.R. Trinkle, Light-element diffusion in Mg using first-principles calculations: anisotropy and elastodiffusion, Phys. Rev. B 94 (2016) 054106.
[81] W.C. Leslie, Iron and its dilue substitutional solid solutions, Metal. Trans. 3 (1972) 5–26.
[82] P. Marinelli, A. Baruj, A.F. Guillermet, M. Sade, Lattice parameters of metastable structures in quenched Fe-Mn alloys. Part I: Experimental techniques, bcc and fcc phases, Z. Metallkd. 91 (2000) 957–962.
[83] P. Marinelli, A. Baruj, A.F. Guillermet, M. Sade, Lattice parameters of metastable structures in quenched Fe-Mn alloys. Part II: hcp phase, Z. Metallkd. 92 (2001) 489–493.
[84] T. Garnier, V.R. Manga, P. Bellon, D.R. Trinkle, Diffusion of Si impurities in Ni under stress: a first-principles study, Phys. Rev. B 90 (2014) 024306.
[85] J.F. Nye, Physical Properties of Crystals: Their Representation by Tensors and Matrices, Oxford University Press, Oxford, 1985.
[86] F. Mouhat, F.-X. Coudert, Necessary and sufficient elastic stability conditions in various crystal systems, Phys. Rev. B 90 (2014) 224104.
[87] T. Kunieda, M. Nakai, Y. Murata, T. Koyama, M. Morinaga, Estimation of the system free energy of martensite phase in an Fe-Cr-C ternary alloy, ISIJ Int. 45 (2005) 1909–1914.
[88] S.-J. Lee, J. Han, C.-Y. Lee, I.-J. Park, Y.-K. Lee, Elastic strain energy induced by epsilon martensitic transformation and its contribution to the stacking-fault energy of austenite in Fe-15Mn-xC alloys, J. Alloys Comp. 617 (2014) 588–596.
[89] Y. Murata, I. Nakaya, M. Morinaga, Assessment of strain energy by measuring dislocation density in copper and aluminium prepared by ECAP and ARB, Mater. Trans. 49 (2008) 20–23.
[90] M. Kehoe, P.M. Kelly, The role of carbon in the strength of ferrous martensite, Scr. Metall. 4 (1970) 473–476.

[91] L.-Å. Nörstrom, On the yield strength of quenched low-carbon lath martensite, Scand. J. Metall. 5 (1976) 159–165.
[92] S. Morito, J. Nishikawa, T. Maki, Dislocation density within lath martensite in Fe-C and Fe-Ni alloys, ISIJ Int. 43 (2003) 1475–1477.
[93] S. Takebayashi, T. Kunieda, N. Yoshinaga, K. Ushioda, S. Ogata, Comparison of the dislocation density in martensitic steels evaluated by some X-ray diffraction methods, ISIJ Int. 50 (2010) 875–882.
[94] R. Meister, L. Peselnick, Variational method of determining effective moduli of polycrystals with tetragonal symmetry, J. Appl. Phys. 37 (1966) 4121–4125.
[95] J.P. Watt, L. Peselnick, Clarification of the Hashin-Shtrikman bounds on the effective elastic moduli of polycrystals with hexagonal, trigonal, and tetragonal symmetries, J. Appl. Phys. 51 (1980) 1525–1531.
[96] S.F. Pugh, Relations between the elastic moduli and the plastic properties of polycrystalline pure metals, Philos. Mag. 45 (1954) 823–843.
[97] G. Wang, S. Shönecker, S. Hertzman, Q.-M. Hu, B. Johansson, S. Kwon, L. Vitos, Ab initio prediction of the mechanical properties of alloys: the case of Ni/Mn doped ferromagnetic Fe, Phys. Rev. B 91 (2015) 224203.